Journal of the Brazilian Society of Mechanical Sciences and Engineering (2021) 43:401
https://doi.org/10.1007/s40430-021-03108-z

TECHNICAL PAPER

Integral transform solution of swirling laminar flows in cylindrical cavities with rotating end walls

Carlos Célio Souza da Cruz[1,2] · Luiz Mariano Pereira[3] · Emanuel Negrão Macêdo[1,4] · João Nazareno Nonato Quaresma[1,4] · Renato Machado Cotta[5,6]

Received: 10 February 2021 / Accepted: 10 July 2021 / Published online: 30 July 2021

Abstract

The present work provides a hybrid numerical–analytical solution through integral transforms for swirling laminar flows of a Newtonian fluid in an end-driven rotating cylindrical cavity. The top-end wall rotates at an angular velocity ω_u, while the bottom-end wall rotates at an angular velocity ω_b, with a fixed sidewall. The Generalized Integral Transform Technique (GITT) is employed to obtain a hybrid solution of the two-dimensional Navier–Stokes equations in the streamfunction-only formulation for steady-state incompressible flow. Results for the velocity components are presented for different aspect ratios (height-to-radius ratio) and Reynolds numbers. The numerical part of the solution is solved through the BVPFD subroutine from the IMSL Library, and the converged results are compared against fully numerical solutions available in the literature, with excellent agreement. In addition, it is shown that the GITT results are in overall agreement with experimental data from the literature. The physical behavior of the computed velocity field is consistent with the experimental flow visualizations regarding position and size of the breakdown bubbles. Finally, the results for both co- and counter-rotation configurations present flow patterns characterized by two symmetric regions that are in accordance with previous findings.

Keywords Swirling flow · Navier–Stokes equations · Cylindrical cavity · Hybrid methods · Integral transforms

List of symbols

A	Aspect ratio ($A = H/R$)
$\bar{f}_i, \bar{g}_i$	Transformed boundary condition coefficients
H	Cylinder height
M_i	Normalization integral, Eq. (42)
N_i	Normalization integral, Eq. (49)
NF, NV	Number of terms in the expansions for the streamfunction and for the tangential velocity component, respectively
P	Pressure
R	Radius of the cylinder
Re	Reynolds number ($\mathrm{Re} = \omega R^2/\nu$)
r, z	Spatial coordinates
s_u, s_b	Rotation dimensionless parameters of the upper and lower ends, respectively
$\bar{v}_{\theta,i}$	Transformed tangential velocity component
v_z	Axial velocity component
v_r	Radial velocity component
v_θ	Tangential velocity component
X_i, Y_i	Eigenfunctions for the streamfunction and the tangential velocity component, respectively
ω_u, ω_b	Angular velocities of the top and bottom-end walls, respectively
γ_i, λ_i	Eigenvalues for the streamfunction and the tangential velocity component, respectively
ν	Kinematic viscosity
Ψ	Streamfunction

Technical Editor: Monica Carvalho.

✉ João Nazareno Nonato Quaresma
quaresma@ufpa.br

1 Graduate Program in Natural Resources Engineering in the Amazon, PRODERNA/ITEC/UFPA, Universidade Federal do Pará, Belém, PA 66075-110, Brazil

2 Science and Technology Program, UFOPA, Universidade Federal do Oeste do Pará, Santarém, PA 68040-470, Brazil

3 Fundação Universidade Federal do Vale do São Francisco, UNIVASF, Petrolina, PE, Brazil

4 School of Chemical Engineering, FEQ/ITEC/UFPA, Universidade Federal do Pará, Belém, PA 66075-110, Brazil

5 Department of Mechanical Engineering, POLI & COPPE/UFRJ, Universidade Federal do Rio de Janeiro, Rio de Janeiro, RJ 21945-970, Brazil

6 General Directorate of Nuclear and Technological Development, DGDNTM, Brazilian Navy, Rio de Janeiro, RJ, Brazil

$\bar{\Psi}_i$	Transformed streamfunction
*	Superscript for dimensional quantities
i, j, k	Subscripts for eigenfunctions indices
$^{-}$	Superscript for transformed quantities

1 Introduction

Studies of rotating fluid flows confined within cylindrical containers have contributed to the development of sophisticated equipment, with improved efficiency, in various technological applications, such as in centrifugal machines, viscometers, turbo-pumps, combustion chambers, heat exchangers, dryers and separators. A typical phenomenon within the framework of rotating flows is the so-called vortex breakdown, which can be defined as an abrupt change of the flow direction in the axial region of the vortex axis, forming one or more recirculation zones and usually affecting the specific application efficiency. This term refers to the disorder characterized by the formation of an internal stagnation point on the vortex axis followed by a reverse flow in a limited axial extension region [1]. Contributions on the occurrence of vortex breakdowns in this type of flow were first presented a few decades ago. In this context, Pao [2] performed a numerical and experimental analysis of a viscous incompressible flow in a closed circular cylindrical cavity. The top and sidewalls rotated at a constant angular velocity, while the base wall remained fixed. Pao [3] numerically evaluated the incompressible viscous fluid flow confined to a closed circular cylindrical cavity with the top disc rotating at a constant angular velocity and the base and sidewalls remaining fixed. An experimental investigation was conducted by Escudier [4], who observed the phenomenon of vortex breakdown in swirling flows within a cylindrical cavity with lower end wall rotation, using a laser-induced fluorescence technique. In the experiment, there were regions of one, two and three vortex-breaking bubbles for certain Reynolds numbers and aspect ratios of the cavity. Escudier [4] then proposed a stability curve and limits for the occurrence of axisymmetric vortex breakdown at different aspect ratios (H/R) and Reynolds numbers.

Even after these pioneering works, theories for vortex breakdown remained somewhat conflicting. For a comprehensive presentation, the reader is referred to the surveys in [1, 5–8], for instance, at different stages of such developments. A comparison of experimentally and numerically determined occurrences of vortex breakdown in swirling flows produced by a rotating end wall can be found in [9]. Experimental visualizations that detected the presence of multiple recirculation zones [4] were compared against numerical simulation. An experimental study was conducted using the laser-induced fluorescence technique to image the flow produced by a continuously rotating bottom wall of an open cylindrical cavity [10]. It was observed that with increasing Reynolds number, the vortex breakdown of the bubbles is directed towards the free surface and the corresponding diameter is increased. The velocity field in a cylindrical cavity due to the rotation of the upper and lower ends with a fixed lateral wall was evaluated in [11]. The characteristic parameters evaluated were the Reynolds number ($Re = 100$–2000) and aspect ratios ($H/R = 0.5$, 0.8, 1.0 and 1.5). It was then concluded that the bubbles stagnation point occurred along the rotation axis, i.e., from the middle of the symmetry plane and the rotating ends of the cavity. This study numerically investigated the steady state, the stability, the initiation of oscillatory instability and transient regimen for the axisymmetric swirling flow of an incompressible Newtonian fluid confined to a circular cylinder closed at the base, with the top rotating independently. Later on [12], the influence of co- and counter-rotation of the base, the vortex breakdown and the beginning of the oscillatory instability were evaluated. The velocity fields were determined for flow in a cavity with independent rotation at both ends [13], examining the formation of bubble recirculation. It was found that, for a range of rotation ratios of the top/bottom walls and a range of Reynolds numbers, the structure and stability of flows were highly sensitive to changes in rotation ratios of the two end walls. The rotating laminar flow within a cylindrical cavity produced by co-rotation of the base and top ends was numerically analyzed in [14]. The steady-state Navier–Stokes equations were solved for various values of the aspect ratio of the cavity, the rotation ratio of the top/bottom walls and the Reynolds number. Experimental measurements of the velocity components were made by Fujimura et al. [15] in a cylindrical cavity with rotation of the upper end wall. The three-dimensional steady-state flow was examined at different aspect ratios and Reynolds numbers. Bhaumik and Lakshmisha [16] investigated the swirling flow due to the upper end wall rotation in a cylindrical cavity to assess the performance of the Lattice Boltzmann Equation approach (LBE) and to further clarify the flow physics. This simulation was compared with experimental and numerical results available in the literature. The Lattice Boltzmann Equation (LBE) formulation was also proposed by Guo et al. [17] for the axisymmetric flow here considered. The proposed model describes the axial, radial and azimuthal velocity components and is proved to be a reliable and efficient method for axisymmetric laminar flows. A lattice Boltzmann model was also proposed by Zhang et al. [18] to simulate axisymmetric incompressible flows. Numerical simulations of Hagen-Poiseuille flow, pulsatile Womersley flow, flow over a sphere and swirling flow in the closed cylindrical cavity were performed. The results were compared with analytical solutions, numerical and experimental results reported in previous studies. Gelfgat

[19] numerically studied the three-dimensional oscillatory instability of the flow in a rotating disk cylinder configuration with aspect ratios between 0.1 and 1. They concluded that the instability could not be described only as instability of the boundary layers near the disks (rotating or stationary disk). Dash and Singh [20] analyzed the numerical simulation of vortex breakdown characteristics in the swirling flow in a cylindrical cavity with an axial rotating rod. They mapped the vortex breakdown zones in the flow as functions of the aspect ratios and Reynolds number. Xiao et al. [21] studied the phenomenon of vortex breakdown in swirling flow with a rotating bottom wall. The energy gradient theory was used to explain the phenomenon in terms of centrifugal and Coriolis forces, angular momentum and azimuthal vorticity. Later, Erkinjon son [22] analyzed the two-phase swirling turbulent flow regarding an air centrifugal separator. Their results were fundamental in powder separation processes.

Despite the availability of numerical solutions based on purely discrete methods for laminar swirling flows, as above discussed, it remains of interest to achieve highly accurate benchmark solutions for the present class of flow problems, so as to provide independent verification of implemented numerical approaches. The Generalized Integral Transform Technique (GITT) [23–29] is a hybrid numerical–analytical approach, well known as a benchmarking tool, which provides accuracy control to some extent only allowed for by an analytical methodology, while offering the applicability span which is more typical of numerical methods. It has been successfully employed in accurately solving various classes of fluid flow problems in channels and cavities governed by the Navier–Stokes equations [30–50], with representative applications in the cylindrical coordinates system [35–37, 43, 47, 49]. For two-dimensional flows, the preferred formulation has been the streamfunction only form of the N–S equations, which leads to the elimination of the pressure field, the automatic satisfaction of the continuity equation and the merging of the momentum balance equations into one single fourth-order nonlinear partial differential equation for the streamfunction field. Then, the related integral transformation process is based on a biharmonic-type fourth-order differential eigenvalue problem, with known analytical solution, while the numerical part of the algorithm involves the solution of a transformed ordinary differential boundary value problem, for steady-state problems, or a transformed ordinary differential initial value problem for transient problems or for pseudo-transient formulations of steady-state problems. The present work aims to demonstrate the GITT approach [23–29] in the hybrid solution of laminar swirling flows, here illustrated for a cylindrical cavity with rotating upper and lower end walls. Convergence analysis for the velocity components fields is performed at different axial and radial positions for various values of the governing parameters, namely the Reynolds number (Re) and the aspect ratio (H/R) of the cavity. For verification and validation of the present solution, critical comparisons are undertaken against computational and experimental results from the literature.

2 Mathematical formulation

The swirling flow characteristics in the closed cylindrical cavity are governed by the Reynolds number ($\mathrm{Re} = \omega R^2/\nu$), where R is the radius of the cylinder, ω is the rotational velocity of the base (ω_b) or top (ω_u) walls, ν is the kinematic viscosity and by the aspect ratio ($A = H/R$), where H is the height of cylinder. The schematic representation of the problem to be analyzed is shown in Fig. 1.

A Newtonian fluid is then rotated inside the container due to the rotating end walls and under the influence of the stationary sidewall. The equations of continuity and conservation of momentum, which model the steady laminar incompressible flow within the cylinder cavity, are written in dimensionless form as:

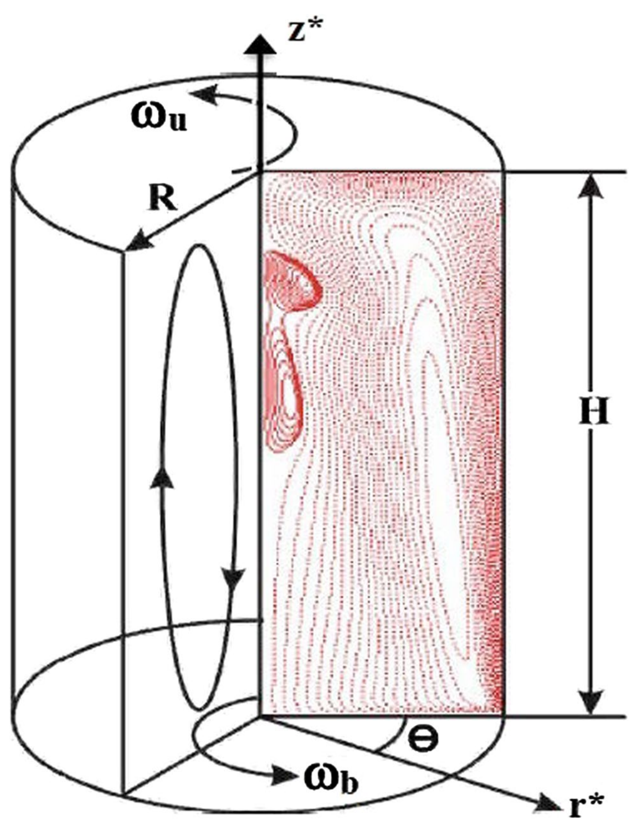

Fig. 1 Schematic representation of the swirling flow problem: geometry of cylindrical cavity with the end walls in rotation

$$\frac{1}{r}\frac{\partial(rv_{\mathrm{r}})}{\partial r}+\frac{\partial v_{\mathrm{z}}}{\partial z}=0 \tag{1}$$

$$v_{\mathrm{r}}\frac{\partial v_{\mathrm{r}}}{\partial r}-\frac{{v_\theta}^2}{r}+v_{\mathrm{z}}\frac{\partial v_{\mathrm{r}}}{\partial z}=-\frac{\partial P}{\partial r}+\frac{1}{\mathrm{Re}}\left[\frac{\partial}{\partial r}\left(\frac{1}{r}\frac{\partial(rv_{\mathrm{r}})}{\partial r}\right)+\frac{\partial^2 v_{\mathrm{r}}}{\partial z^2}\right] \tag{2}$$

$$v_{\mathrm{r}}\frac{\partial v_{\mathrm{z}}}{\partial r}+v_{\mathrm{z}}\frac{\partial v_{\mathrm{z}}}{\partial z}=-\frac{\partial P}{\partial z}+\frac{1}{\mathrm{Re}}\left[\frac{1}{r}\frac{\partial}{\partial r}\left(r\frac{\partial v_{\mathrm{z}}}{\partial r}\right)+\frac{\partial^2 v_{\mathrm{z}}}{\partial z^2}\right] \tag{3}$$

$$v_{\mathrm{r}}\frac{\partial v_\theta}{\partial r}+\frac{v_{\mathrm{r}}v_\theta}{r}+v_{\mathrm{z}}\frac{\partial v_\theta}{\partial z}=\frac{1}{\mathrm{Re}}\left[\frac{\partial}{\partial r}\left(\frac{1}{r}\frac{\partial(rv_\theta)}{\partial r}\right)+\frac{\partial^2 v_\theta}{\partial z^2}\right] \tag{4}$$

The dimensionless boundary conditions are given by:

$$v_{\mathrm{r}}(0,z)=0;\;\; v_\theta(0,z)=0;\;\; \frac{\partial v_{\mathrm{z}}(0,z)}{\partial r}=0 \tag{5--7}$$

$$v_{\mathrm{r}}(1,z)=0;\;\; v_\theta(1,z)=0;\;\; v_{\mathrm{z}}(1,z)=0 \tag{8--10}$$

$$v_{\mathrm{r}}(r,0)=0; v_\theta(r,0)=s_{\mathrm{b}}r; v_{\mathrm{z}}(r,0)=0 \tag{11--13}$$

$$v_{\mathrm{r}}(r,A)=0; v_\theta(r,A)=s_{\mathrm{u}}r; v_{\mathrm{z}}(r,A)=0 \tag{14--16}$$

The following dimensionless groups were employed to obtain Eqs. (1–16):

$$\begin{aligned}&r=\frac{r^*}{R};z=\frac{z^*}{R};A=\frac{H}{R};s_b=\frac{\omega_b}{\omega};s_u=\frac{\omega_u}{\omega};\\&P=\frac{P^*}{\rho R^2\omega^2};v_{\mathrm{r}}=\frac{v_{\mathrm{r}}^*}{R\omega};v_{\mathrm{z}}=\frac{v_{\mathrm{z}}^*}{R\omega};v_\theta=\frac{v_\theta^*}{R\omega}\end{aligned} \tag{17a--i}$$

The streamfunction is defined in terms of the velocity components in the r and z directions as:

$$v_{\mathrm{r}}=\frac{1}{r}\frac{\partial\psi}{\partial z};v_{\mathrm{z}}=-\frac{1}{r}\frac{\partial\psi}{\partial r} \tag{18a, b}$$

Therefore, with the use of the streamfunction definition given by Eqs. (18), the continuity equation, Eq. (1), is automatically satisfied. On the other hand, the radial and axial momentum equations are manipulated, differentiating each one by, respectively, the axial and radial coordinates, so as to eliminate the pressure field while merging these momentum balance equations into a single equation for the new dependent variable, ψ. Then, the streamfunction equation and the tangential momentum balance equation, together with their respective boundary conditions, are written as [49]:

$$\frac{1}{r}\frac{\partial\psi}{\partial z}\frac{\partial(E^2\psi)}{\partial r}-\frac{1}{r}\frac{\partial\psi}{\partial r}\frac{\partial(E^2\psi)}{\partial z}-\frac{2}{r^2}\frac{\partial\psi}{\partial z}E^2\psi-2v_\theta\frac{\partial v_\theta}{\partial z}=\frac{1}{\mathrm{Re}}E^4\psi \tag{19}$$

$$\frac{1}{r}\frac{\partial\psi}{\partial z}\left(\frac{\partial v_\theta}{\partial r}+\frac{v_\theta}{r}\right)-\frac{1}{r}\frac{\partial\psi}{\partial r}\frac{\partial v_\theta}{\partial z}=\frac{1}{\mathrm{Re}}\left(\frac{\partial^2 v_\theta}{\partial r^2}+\frac{1}{r}\frac{\partial v_\theta}{\partial r}-\frac{v_\theta}{r^2}-\frac{\partial^2 v_\theta}{\partial z^2}\right) \tag{20}$$

$$\underset{r\to 0}{Lim}\left[\frac{\psi(r,z)}{r}\right]=0;\ \underset{r\to 0}{Lim}\left\{\frac{\partial}{\partial r}\left[\frac{1}{r}\frac{\partial\psi(r,z)}{\partial r}\right]\right\}=0; v_\theta(0,z)=0 \tag{21--23}$$

$$\psi(1,z)=0;\;\; \frac{\partial\psi(1,z)}{\partial r}=0;\;\; v_\theta(1,z)=0 \tag{24--26}$$

$$\psi(r,0)=0;\;\; \frac{\partial\psi(r,0)}{\partial z}=0; v_\theta(r,0)=s_b r \tag{27--29}$$

$$\psi(r,A)=0;\;\; \frac{\partial\psi(r,A)}{\partial z}=0;\;\; v_\theta(r,A)=s_u r \tag{30--32}$$

where the associated operators E^2 and E^4 are defined as:

$$\begin{aligned}&E^2=\frac{\partial^2}{\partial r^2}-\frac{1}{r}\frac{\partial}{\partial r}+\frac{\partial^2}{\partial z^2}\\&E^4=E^2(E^2)=\frac{\partial^4}{\partial r^4}-\frac{2}{r}\frac{\partial^3}{\partial r^3}+\frac{3}{r^2}\frac{\partial^2}{\partial r^2}\\&\quad-\frac{3}{r^3}\frac{\partial}{\partial r}-\frac{2}{r}\frac{\partial^3}{\partial r\partial z^2}+2\frac{\partial^4}{\partial r^2\partial z^2}+\frac{\partial^4}{\partial z^4}\end{aligned} \tag{33a, b}$$

3 Solution methodology

The Generalized Integral Transform Technique (GITT) [23–29] is a hybrid numerical–analytical solution methodology, well known for providing error-controlled results in different applications involving diffusion and convection–diffusion processes. The relative merits of this technique are in fact due to its hybrid nature, both in terms of low computational cost and high attainable accuracy. In this approach, the integral transformation process in general eliminates all but one of the independent variables. Thus, an analytical solution is determined through the proposed eigenfunction expansion for all the independent variables eliminated through integral transformation, while for that only variable is not eliminated, the solution is numerically obtained from the resulting ordinary differential system derived from the integral transformation process of the original partial differential equations. Therefore, following the GITT formalism, the first task is to choose appropriate eigenvalue problems for the eigenfunction expansions for the streamfunction and for the tangential velocity component, which are here chosen as [43, 47, 49]

For the streamfunction:

$$\left(\frac{\mathrm{d}^4}{\mathrm{d}r^4}-\frac{2}{r}\frac{\mathrm{d}^3}{\mathrm{d}r^3}+\frac{3}{r^2}\frac{\mathrm{d}^2}{\mathrm{d}r^2}-\frac{3}{r^3}\frac{\mathrm{d}}{\mathrm{d}r}\right)X_i(r)=-\gamma_i^2\left[r\frac{\mathrm{d}}{\mathrm{d}r}\left(\frac{1}{r}\frac{\mathrm{d}}{\mathrm{d}r}\right)\right]X_i(r) \tag{34}$$

$$\lim_{r\to 0}\left[\frac{X_i(r)}{r}\right]=0;\ \lim_{r\to 0}\left\{\frac{d}{dr}\left[\frac{1}{r}\frac{dX_i(r)}{dr}\right]\right\}=0 \qquad (35, 36)$$

$$X_i(1)=0;\ \frac{dX_i(1)}{dr}=0 \qquad (37, 38)$$

The eigenvalue problem given by Eqs. (34–38) is a biharmonic type differential equation, and its solution is given by:

$$X_i(r)=r^2-\frac{rJ_1(\gamma_i r)}{J_1(\gamma_i)} \qquad (39)$$

where the eigenvalues, γ_i, are calculated from the following transcendental equation:

$$J_2(\gamma_i)=0,\quad i=1,2,3,\ldots \qquad (40)$$

The eigenfunctions, X_i(r), satisfy the following orthogonality property:

$$\int_0^1 \frac{1}{r}\frac{dX_i(r)}{dr}\frac{dX_j(r)}{dr}dr=\begin{cases}0, & i\neq j\\ M_i, & i=j\end{cases};\ M_i=\int_0^1\frac{1}{r}\left[\frac{dX_i(r)}{dr}\right]^2dr=\frac{\gamma_i^2}{2} \qquad (41, 42)$$

For the tangential velocity component:

$$\frac{1}{r}\frac{d}{dr}\left[r\frac{dY_i(r)}{dr}\right]-\left(\frac{1}{r^2}-\lambda_i^2\right)Y_i(r)=0 \qquad (43)$$

$$Y_i(0)=0;\quad Y_i(1)=0 \qquad (44, 45)$$

The analytical solution of the eigenvalue problem given by Eqs. (43–45) is obtained as:

$$Y_i(r)=J_1(\lambda_i r) \qquad (46)$$

with the eigenvalues, λ_i, calculated from the transcendental equation:

$$J_1(\lambda_i)=0,\quad i=1,2,3,\ldots \qquad (47)$$

The eigenfunctions, Y_i(r), enjoy the following orthogonality property:

$$\int_0^1 rY_i(r)Y_j(r)dr=\begin{cases}0, & i\neq j\\ N_i, & i=j\end{cases};\ N_i=\int_0^1 rY_i^2(r)dr=\frac{J_0^2(\lambda_i)}{2} \qquad (48, 49)$$

After the choice of suitable eigenvalue problems, the next step is to define the integral transform pairs, here taken as:

$$\overline{\psi}_i(z)=-\frac{1}{M_i}\int_0^1\left[\frac{d}{dr}\left(\frac{1}{r}\frac{dX_i(r)}{dr}\right)\right]\psi(r,z)dr,\quad \text{transform} \qquad (50)$$

$$\psi(r,z)=\sum_{i=1}^{\infty}X_i(r)\overline{\psi}_i(z),\quad \text{inverse} \qquad (51)$$

$$\overline{v}_{\theta,i}(z)=\frac{1}{N_i}\int_0^1 rY_i(r)v_\theta(r,z)dr,\quad \text{transform} \qquad (52)$$

$$v_\theta(r,z)=\sum_{i=1}^{\infty}Y_i(r)\overline{v}_{\theta,i}(z),\quad \text{inverse} \qquad (53)$$

The next task is to promote the integral transformation of the partial differential system given by Eqs. (19–32). For this purpose, Eqs. (19) and (20) and the boundary conditions (27–32) are multiplied by $X_i(r)/r$ and rY_i(r), respectively, and then integrated over the domain [0,1] in the radial direction. The inverse formulae given by Eqs. (51) and (53) are employed in place of the potentials. After the required manipulations, the following coupled ordinary differential system for determining the transformed potentials is obtained:

$$\sum_{j=1}^{\infty}A_{ij}\frac{d^4\overline{\psi}_j(z)}{dz^4}=\gamma_i^2\frac{d^2\overline{\psi}_i(z)}{dz^2}-\frac{\gamma_i^2}{2}\overline{\psi}_i(z)+\mathrm{Re}\left\{\sum_{j=1}^{\infty}\sum_{k=1}^{\infty}\left[B_{ijk}\overline{\psi}_j(z)\frac{d\overline{\psi}_k(z)}{dz}+C_{ijk}\frac{d\overline{\psi}_j(z)}{dz}\frac{d^2\overline{\psi}_k(z)}{dz^2}+D_{ijk}\overline{\psi}_j(z)\frac{d^3\overline{\psi}_k(z)}{dz^3}\right]+\sum_{j=1}^{\infty}\sum_{k=1}^{\infty}E_{ijk}\overline{v}_{\theta,j}(z)\frac{d\overline{v}_{\theta,k}(z)}{dz}\right\} \qquad (54)$$

$$\frac{d^2\overline{v}_{\theta,i}(z)}{dz^2}=\lambda_i^2\overline{v}_{\theta,i}(z)+\mathrm{Re}\sum_{j=1}^{\infty}\sum_{k=1}^{\infty}\left[F_{ijk}\overline{v}_{\theta,j}(z)\frac{d\overline{\psi}_k(z)}{dz}+G_{ijk}\frac{d\overline{v}_{\theta,j}(z)}{dz}\overline{\psi}_k(z)\right] \qquad (55)$$

$$\overline{\psi}_i(0)=0;\quad \frac{d\overline{\psi}_i(0)}{dz}=0;\ \overline{v}_{\theta,i}(0)=\overline{f}_i \qquad (56–58)$$

$$\overline{\psi}_i(A)=0;\quad \frac{d\overline{\psi}_i(A)}{dz}=0;\ \overline{v}_{\theta,i}(A)=\overline{g}_i \qquad (59–61)$$

where various integral coefficients in the above transformed system are given by:

$$A_{\mathrm{ij}} = \int_0^1 \frac{X_{\mathrm{i}}(r)X_{\mathrm{j}}(r)}{r}\mathrm{d}r,$$

$$B_{\mathrm{ijk}} = \int_0^1 X_{\mathrm{i}}(r)\left\{\left[\frac{1}{r^2}\frac{\mathrm{d}^3X_j(r)}{\mathrm{d}r^3} - \frac{3}{r^3}\frac{d^2X_j(r)}{\mathrm{d}r^2} + \frac{3}{r^4}\frac{\mathrm{d}X_j(r)}{\mathrm{d}r}\right]X_{\mathrm{k}}(r) - \frac{1}{r^2}\frac{\mathrm{d}X_j(r)}{\mathrm{d}r}\frac{\mathrm{d}^2X_{\mathrm{k}}(r)}{\mathrm{d}r^2} + \frac{1}{r^3}\frac{\mathrm{d}X_j(r)}{\mathrm{d}r}\frac{\mathrm{d}X_k(r)}{\mathrm{d}r}\right\}\mathrm{d}r \quad (62, 63)$$

$$C_{\mathrm{ijk}} = \int_0^1 X_{\mathrm{i}}(r)\left[\frac{X_j(r)}{r^2}\frac{\mathrm{d}X_{\mathrm{k}}(r)}{\mathrm{d}r} - \frac{2}{r^3}X_{\mathrm{j}}(r)X_{\mathrm{k}}(r)\right]\mathrm{d}r,$$

$$D_{\mathrm{ijk}} = -\int_0^1 \frac{X_{\mathrm{i}}(r)}{r^2}\frac{dX_j(r)}{\mathrm{d}r}X_k(r)\mathrm{d}r \quad (64, 65)$$

$$E_{\mathrm{ijk}} = -2\int_0^1 \frac{X_{\mathrm{i}}(r)Y_{\mathrm{j}}(r)Y_{\mathrm{k}}(r)}{r}\mathrm{d}r,$$

$$F_{\mathrm{ijk}} = \frac{1}{N_{\mathrm{i}}}\int_0^1 Y_{\mathrm{i}}(r)\left[\frac{\mathrm{d}Y_j(r)}{\mathrm{d}r} + \frac{Y_{\mathrm{j}}(r)}{r}\right]X_k(r)\mathrm{d}r \quad (66, 67)$$

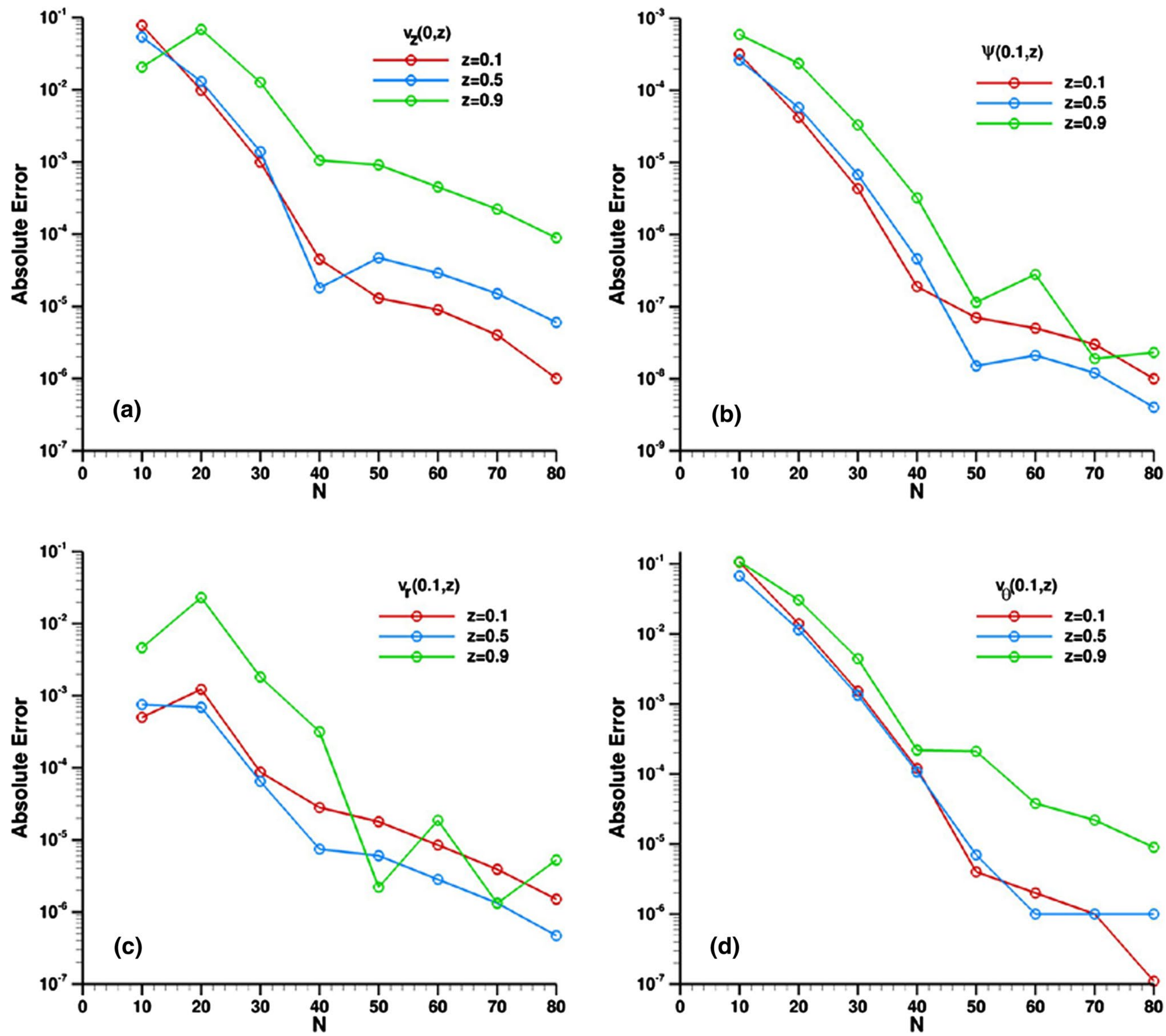

Fig. 2 Absolute errors variation for increasing truncation orders at different axial positions for Re = 2000 and A = 1.0: **a** $v_z(0,z)$; **b** $\psi(0.1,z)$; **c** $v_r(0.1,z)$; **d** $v_\theta(0.1,z)$. Reference solution computed with N = 90 terms

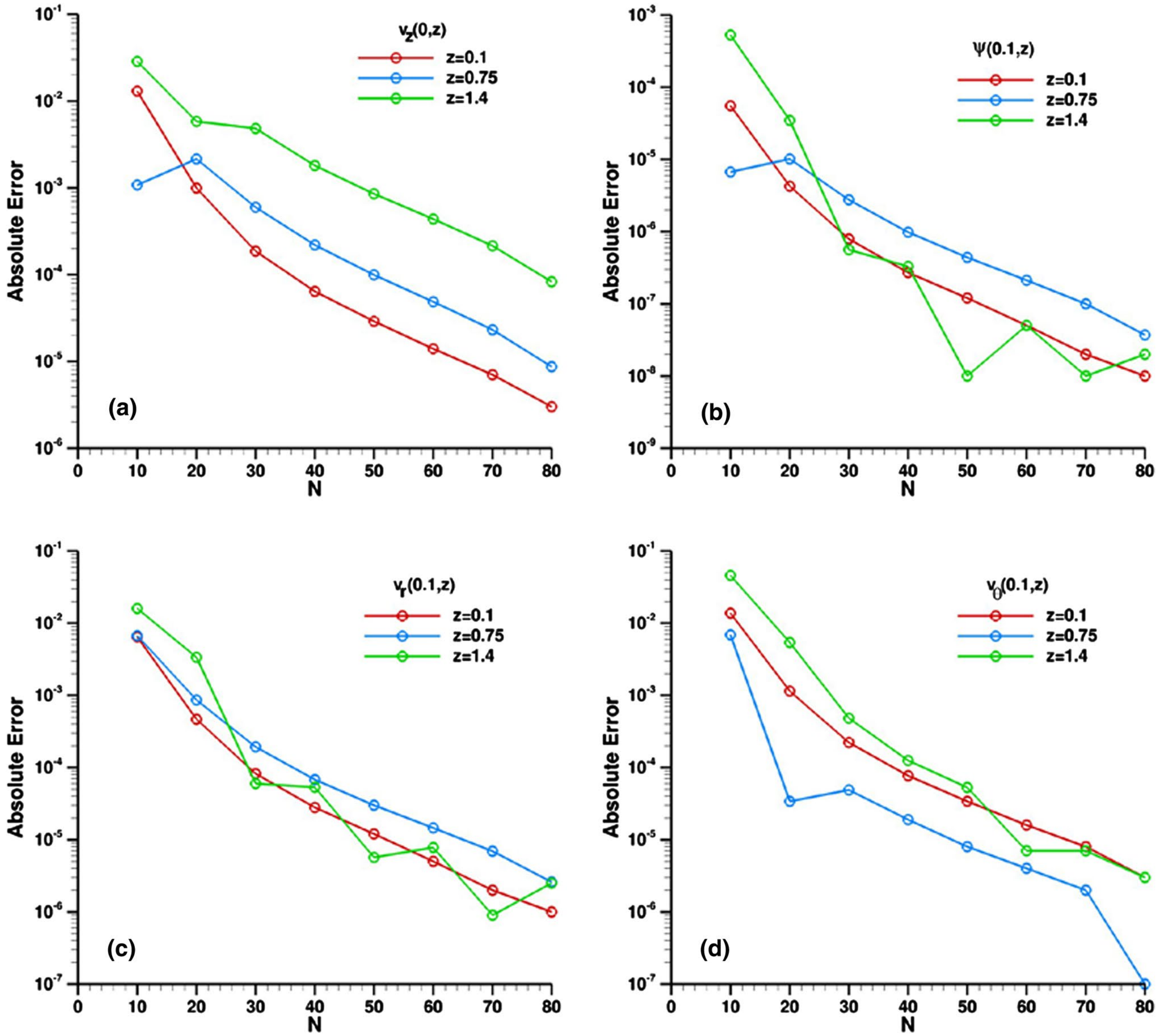

Fig. 3 Absolute errors variation for increasing truncation orders at different axial positions for Re = 990 and $A = 1.5$: **a** $v_z(0,z)$; **b** $\psi(0.1,z)$; **c** $v_r(0.1,z)$; **d** $v_\theta(0.1,z)$. Reference solution computed with $N = 90$ terms

$$G_{\mathrm{ijk}} = -\frac{1}{N_i}\int_0^1 Y_i(r)Y_j(r)\frac{\mathrm{d}X_k(r)}{\mathrm{d}r}\mathrm{d}r,$$

$$\bar{f}_i = \frac{s_b}{N_i}\int_0^1 r^2 Y_i(r)\mathrm{d}r, \quad \bar{g}_i = \frac{s_u}{N_i}\int_0^1 r^2 Y_i(r)\mathrm{d}r \qquad (68\text{–}70)$$

To numerically handle the ODE system given by Eqs. (54–61), subroutine BVPFD of the IMSL Library [51] is employed. It is then necessary to truncate the infinite system, by truncating the expansions to a sufficiently large number of terms (NF for the streamfunction and NV for the tangential velocity expansions), so as to guarantee the desired overall relative error control in obtaining the original potentials. This subroutine solves a parameterized system of ordinary differential equations with boundary conditions at two points using a variable order, variable step-size finite difference method with deferred corrections. It also provides the important feature of automatically controlling the relative error in the solution of the ODE system, thus allowing the user to establish error targets for the transformed potentials.

Table 1 Convergence of axial velocity component, streamfunction, radial and tangential velocity components for radial positions $r=0$ and 0.1, and for $\mathrm{Re}=2000$ and $A=1.0$

$r=0$						
Axial velocity						
z	$N=10$	$N=20$	$N=40$	$N=60$	$N=80$	$N=90$
0.1	0.101	0.325×10^{-1}	0.228×10^{-1}	0.227×10^{-1}	0.227×10^{-1}	0.227×10^{-1}
0.5	0.710×10^{-1}	0.301×10^{-1}	0.171×10^{-1}	0.171×10^{-1}	0.171×10^{-1}	0.171×10^{-1}
0.9	0.375×10^{-1}	0.855×10^{-1}	0.158×10^{-1}	0.165×10^{-1}	0.168×10^{-1}	0.169×10^{-1}
$r=0.1$						
Streamfunction						
z	$N=10$	$N=20$	$N=40$	$N=60$	$N=80$	$N=90$
0.1	-0.435×10^{-3}	-0.160×10^{-3}	-0.117×10^{-3}	-0.117×10^{-3}	-0.117×10^{-3}	-0.117×10^{-3}
0.5	-0.351×10^{-3}	-0.145×10^{-3}	-0.874×10^{-4}	-0.869×10^{-4}	-0.869×10^{-4}	-0.869×10^{-4}
0.9	-0.680×10^{-3}	-0.324×10^{-3}	-0.896×10^{-4}	-0.864×10^{-4}	-0.864×10^{-4}	-0.863×10^{-4}
Radial velocity						
z	$N=10$	$N=20$	$N=40$	$N=60$	$N=80$	$N=90$
0.1	-0.738×10^{-2}	-0.811×10^{-2}	-0.685×10^{-2}	-0.687×10^{-2}	-0.688×10^{-2}	-0.688×10^{-2}
0.5	-0.140×10^{-3}	-0.784×10^{-4}	0.623×10^{-3}	0.619×10^{-3}	0.616×10^{-3}	0.616×10^{-3}
0.9	-0.385×10^{-2}	-0.224×10^{-1}	0.475×10^{-3}	0.772×10^{-3}	0.786×10^{-3}	0.791×10^{-3}
Tangential velocity						
z	$N=10$	$N=20$	$N=40$	$N=60$	$N=80$	$N=90$
0.1	0.146	0.540×10^{-1}	0.401×10^{-1}	0.400×10^{-1}	0.400×10^{-1}	0.400×10^{-1}
0.5	0.971×10^{-1}	0.409×10^{-1}	0.296×10^{-1}	0.295×10^{-1}	0.295×10^{-1}	0.295×10^{-1}
0.9	0.135	0.579×10^{-1}	0.276×10^{-1}	0.273×10^{-1}	0.273×10^{-1}	0.273×10^{-1}

N = NF = NV

4 Results and discussion

A computer code was developed in the FORTRAN 2003 programming language and implemented on an Intel Core i7 3.07 GHz desktop computer. The routine BVPFD from the IMSL Library [51] was used to numerically handle the truncated version of the ordinary differential system, Eqs. (54–61), with a prescribed relative error target of 10^{-4} (four significant digits) for the transformed potentials. The analyses were performed for the case of stationary lower end and rotating upper end, i.e., ($s_u=1$ and $s_b=0$), except when indicated in the figure captions.

A brief convergence analysis on the streamfunction, axial, radial, and tangential velocity components was performed, illustrating the eigenfunction expansions behavior, considering the following values of the Reynolds number and of the aspect ratio: $\mathrm{Re}=2000$ and $A=H/R=1.0$ (Fig. 2) and $\mathrm{Re}=990$ and $A=H/R=1.5$ (Fig. 3). For this purpose, the absolute error in each expansion, for increasing truncation orders to within $\mathrm{NT}\leq 80$, was calculated by adopting $\mathrm{NT}=90$ as the maximum truncation order taken as the reference solution. It can be seen from both figures that the absolute error of the results for all four potentials confirms the excellent convergence rates, achieving convergence within truncation orders below N = NF = NV = 80 terms, in each expansion, for all r and z positions reported. It can be observed that the convergences of the streamfunction and of the tangential velocity component occur with a smaller number of terms in the expansions than those required for the radial and axial components, when considering the same positions within the cavity section. This overall behavior occurs because Eqs. (18) that relate the radial and axial velocity components to the streamfunction are calculated from the derivatives of the streamfunction with respect to the coordinates z and r, respectively, which bring the eigenvalues to the numerator of the expansions, and the convergence is then expected to be slowed down in comparison with those of the streamfunction and tangential velocity, evaluated from direct expansions (Eqs. (51) and (53)). Tables 1 and 2 provide a set of reference results for these quantities and for the same two cases, namely $\mathrm{Re}=2000$ and $A=H/R=1.0$ (Table 1) and $\mathrm{Re}=990$ and $A=H/R=1.5$ (Table 2). It can be

Table 2 Convergence of axial velocity component, streamfunction, radial and tangential velocity components for radial positions $r=0$ and 0.1, and for Re = 990 and $A=1.5$

$r=0$						
Axial velocity						
z	$N=10$	$N=20$	$N=40$	$N=60$	$N=80$	$N=90$
0.1	0.490×10^{-1}	0.369×10^{-1}	0.360×10^{-1}	0.359×10^{-1}	0.359×10^{-1}	0.359×10^{-1}
0.75	0.662×10^{-2}	0.555×10^{-2}	0.748×10^{-2}	0.765×10^{-2}	0.769×10^{-2}	0.770×10^{-2}
1.4	0.517×10^{-1}	0.173×10^{-1}	0.212×10^{-1}	0.226×10^{-1}	0.229×10^{-1}	0.230×10^{-1}
$r=0.1$						
Stream function						
z	$N=10$	$N=20$	$N=40$	$N=60$	$N=80$	$N=90$
0.1	-0.220×10^{-3}	-0.169×10^{-3}	-0.165×10^{-3}	-0.165×10^{-3}	-0.164×10^{-3}	-0.164×10^{-3}
0.75	-0.445×10^{-4}	-0.411×10^{-4}	-0.503×10^{-4}	-0.510×10^{-4}	-0.512×10^{-4}	-0.512×10^{-4}
1.4	-0.643×10^{-3}	-0.151×10^{-3}	-0.117×10^{-3}	-0.117×10^{-3}	-0.117×10^{-3}	-0.116×10^{-3}
Radial velocity						
z	$N=10$	$N=20$	$N=40$	$N=60$	$N=80$	$N=90$
0.1	-0.302×10^{-1}	-0.242×10^{-1}	-0.238×10^{-1}	-0.238×10^{-1}	-0.238×10^{-1}	-0.238×10^{-1}
0.75	-0.254×10^{-2}	0.332×10^{-2}	0.411×10^{-2}	0.416×10^{-2}	0.418×10^{-2}	0.418×10^{-2}
1.4	-0.125×10^{-1}	0.374×10^{-3}	0.369×10^{-2}	0.373×10^{-2}	0.374×10^{-2}	0.374×10^{-2}
Tangential velocity						
z	$N=10$	$N=20$	$N=40$	$N=60$	$N=80$	$N=90$
0.1	0.478×10^{-1}	0.352×10^{-1}	0.341×10^{-1}	0.341×10^{-1}	0.340×10^{-1}	0.340×10^{-1}
0.75	0.186×10^{-1}	0.117×10^{-1}	0.117×10^{-1}	0.117×10^{-1}	0.117×10^{-1}	0.117×10^{-1}
1.4	0.676×10^{-1}	0.270×10^{-1}	0.216×10^{-1}	0.217×10^{-1}	0.217×10^{-1}	0.217×10^{-1}

N = NF = NV

Table 3 Comparison of the axial maximum velocity for different Reynolds numbers and aspect ratios at $r=0$

Reference	Re = 990 and		Re = 1010 and		Re = 1290 and	
	$A=1.5$		$A=2.5$		$A=1.5$	
	$v_{z,max}$	h_{max}/H	$v_{z,max}$	h_{max}/H	$v_{z,max}$	h_{max}/H
GITT (present)	0.0986	0.207	0.103	0.445	0.0704	0.142
Experimental [15]	0.097	0.21	0.103	0.46	0.068	0.14
3D LBM [16]	0.093	0.22	0.102	0.52	0.072	0.16
FVM N-S [16]	0.099	0.19	0.106	0.44	0.0665	0.125
% deviation GITTxExperimental	1.65%	−1.43%	0.0%	−3.26%	3.53%	1.43%

seen from both tables that the results for all four potentials achieve convergence to at least three significant digits within truncation orders below N = NF = NV = 90 terms, in each expansion, for all r and z positions reported.

The maximum value of the axial velocity component ($v_{z,max}$) and the position of its occurrence (h_{max}/H) are shown in Table 3, for Re = 990 and $A=1.5$, Re = 1010 and $A=2.5$, and Re = 1290 and $A=1.5$, at $r=0$, and compared with experimental data [15], with a simulation based on the 3D lattice Boltzmann method (LBM) and with the finite volume method solution of the Navier–Stokes equations (FVM N–S), both numerical solutions extracted from the work of Bhaumik and Lakshmisha [16]. The relative deviations between numerical solutions and experimental measurements were calculated from $\varepsilon=(v_{z,num}-v_{z,exp})/v_{z,exp}$. Table 3 shows that the overall agreement of the GITT solution with

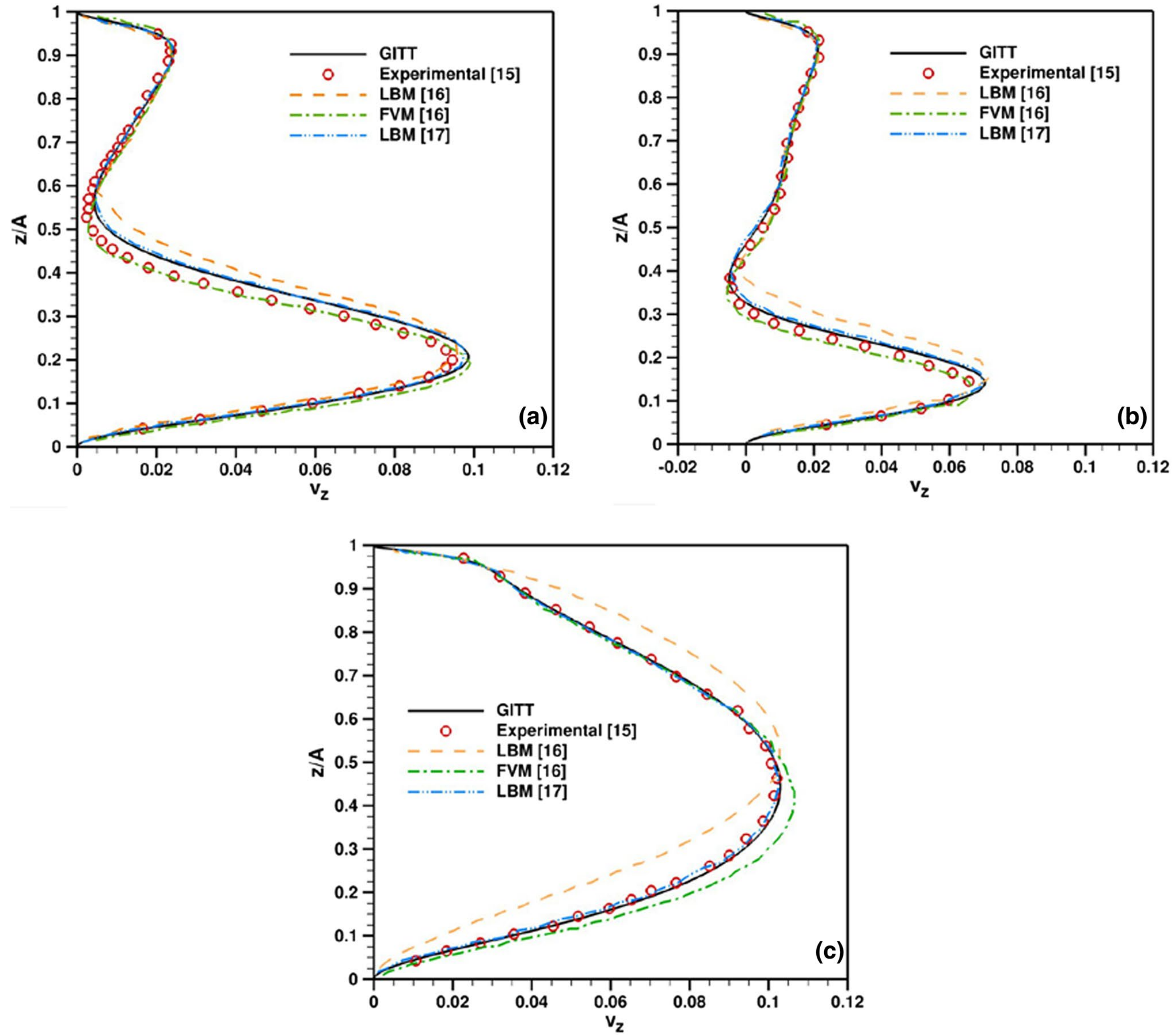

Fig. 4 Profile of the axial velocity component at $r=0$: **a** $\mathrm{Re}=990$ and $A=1.5$; **b** $\mathrm{Re}=1290$ and $A=1.5$; **c** $\mathrm{Re}=1010$ and $A=2.5$

the experimental results for the maximum velocity component and its dimensionless location is indeed very good, being roughly below 3.5% for both the maximum velocity value and its location, for all the Reynolds numbers here considered.

The behavior of the axial velocity component in the axisymmetric rotational flow is shown in Fig. 4. This figure compares the results obtained via GITT against those obtained experimentally [15] and numerically [16, 17]. The profiles are taken at $r=0$ for the axial velocity component, again emphasizing the previously considered cases, $\mathrm{Re}=990$ and $A=1.5$, $\mathrm{Re}=1290$ and $A=1.5$, and $\mathrm{Re}=1010$ and $A=2.5$. First, by performing a graphical comparison of the results for the axial velocity, the results obtained by GITT, for all cases studied, can be seen to be in excellent agreement with the LBM solution in ref. [17]. The solution obtained by GITT also shows good agreement with the LBM and FVM solutions [16] and with the experimental data [15] for Fig. 4a, b. In Fig. 4.c, however, for $\mathrm{Re}=1010$ and $A=2.5$, the GITT approach agrees very well with the experimental [15] and LBM results [17], while the results of the FVM and 3D-LBM simulations [16] are less adherent to those of GITT, LBM [17] and the experimental data [15]. The present results also confirmed that the so-called vortex breakdown does occur at $\mathrm{Re}=1010$ and $A=1.5$, while for $\mathrm{Re}=990$ and $A=1.5$ and for $\mathrm{Re}=1290$ and $A=2.5$, this breakdown does not occur.

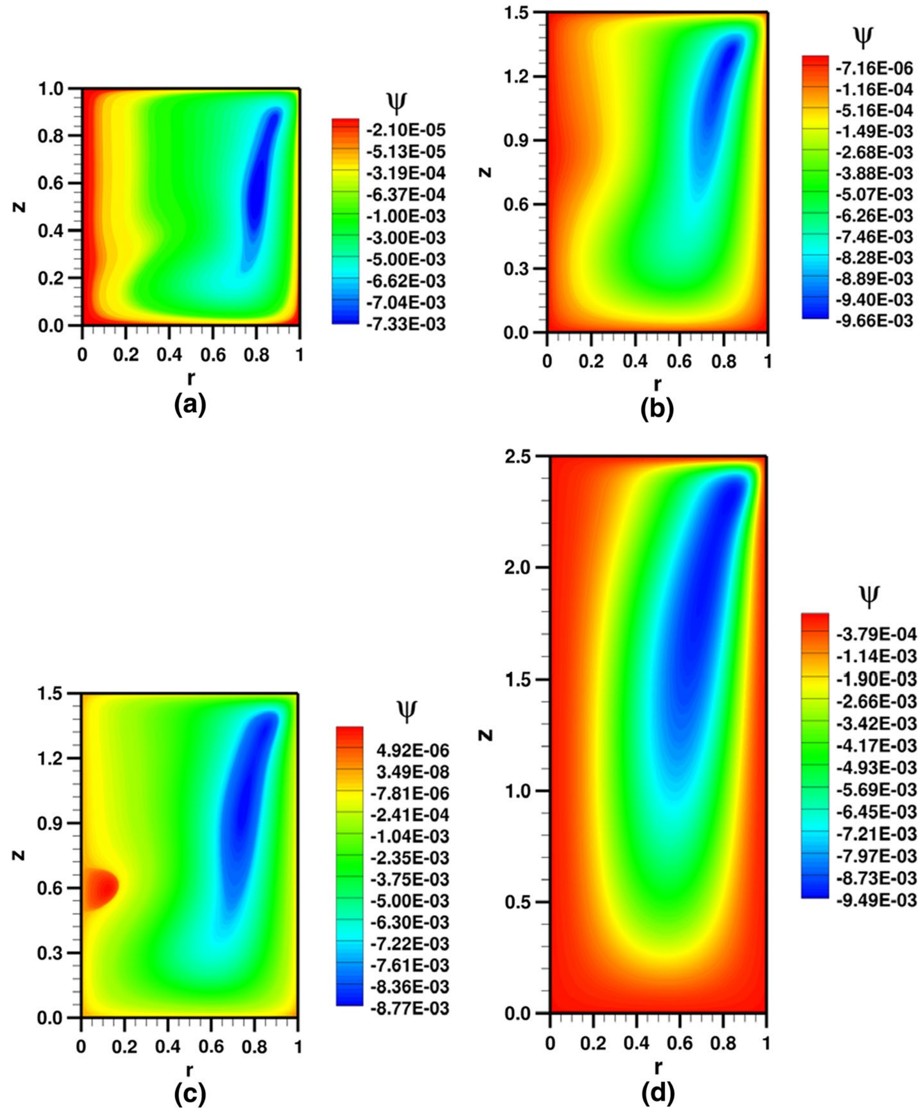

Fig. 5 Contour plots of streamfunction: **a** Re = 2000 and $A = 1.0$; **b** Re = 990 and $A = 1.5$; **c** Re = 1290 and $A = 1.5$; **d** Re = 1010 and $A = 2.5$

Figure 5 illustrates the behavior of the streamfunction as obtained through GITT, with contour plots presented for different Reynolds numbers and aspect ratios. According to the Escudier's regime diagram [4], also confirmed by Bhaumik and Lakshmisha [16], the results in Fig. 5a, b, d do not lead to vortex breakdown. In these conditions, the central vortex has a small thickness in the region near the lower end, and it increases when approaching the rotating lid with the formation of the Ekman boundary layer. Thus, the Coriolis force has predominance over the pressure gradient, forcing mass transport to the lateral wall and forming a low-pressure region in the center of the rotating lid. Moreover, the flow behavior illustrated in Fig. 5c (Re = 1290 and $A = 1.5$) exhibits a single vortex breakdown. Therefore, the predicted results from GITT simulations are consistent with the numerical work of Bhaumik and Lakshmisha [16] and with Escudier's regime diagram [4].

Figure 6a–c also provides contour plots of the streamfunction aimed at comparisons against the experimental results obtained by Escudier [4], where the phenomenon of vortex breakdown was first documented. The GITT results here presented are in overall agreement with the experimental results of Escudier [4]. As in ref. [4], it has been observed that for $H/R = 2$ and Re = 1854 (Fig. 6a), the upper bubble decreases and arises another vortex breakdown with smaller bubbles and the hourglass form of the vortex core predicts the appearance of a second breakdown. As shown in Fig. 6b, c, with the increase in both Reynolds number and aspect ratio, there is the appearance of three breakdown bubbles. For instance, in Fig. 6b it can be visualized three vortex breakdown structures, two coupled in the central part and a separated one further above, as also observed from the experimental results.

In Figs. 7 and 8 are presented the streamfunction contours induced by co- and counter-rotation of the end walls for

Fig. 6 Contour plots of stream-function ($s_u = 0$ and $s_b = -1$): **a** Re = 1854 and $A = 2.0$; **b** Re = 2819 and $A = 3.25$; **c** Re = 3061 and $A = 3.5$

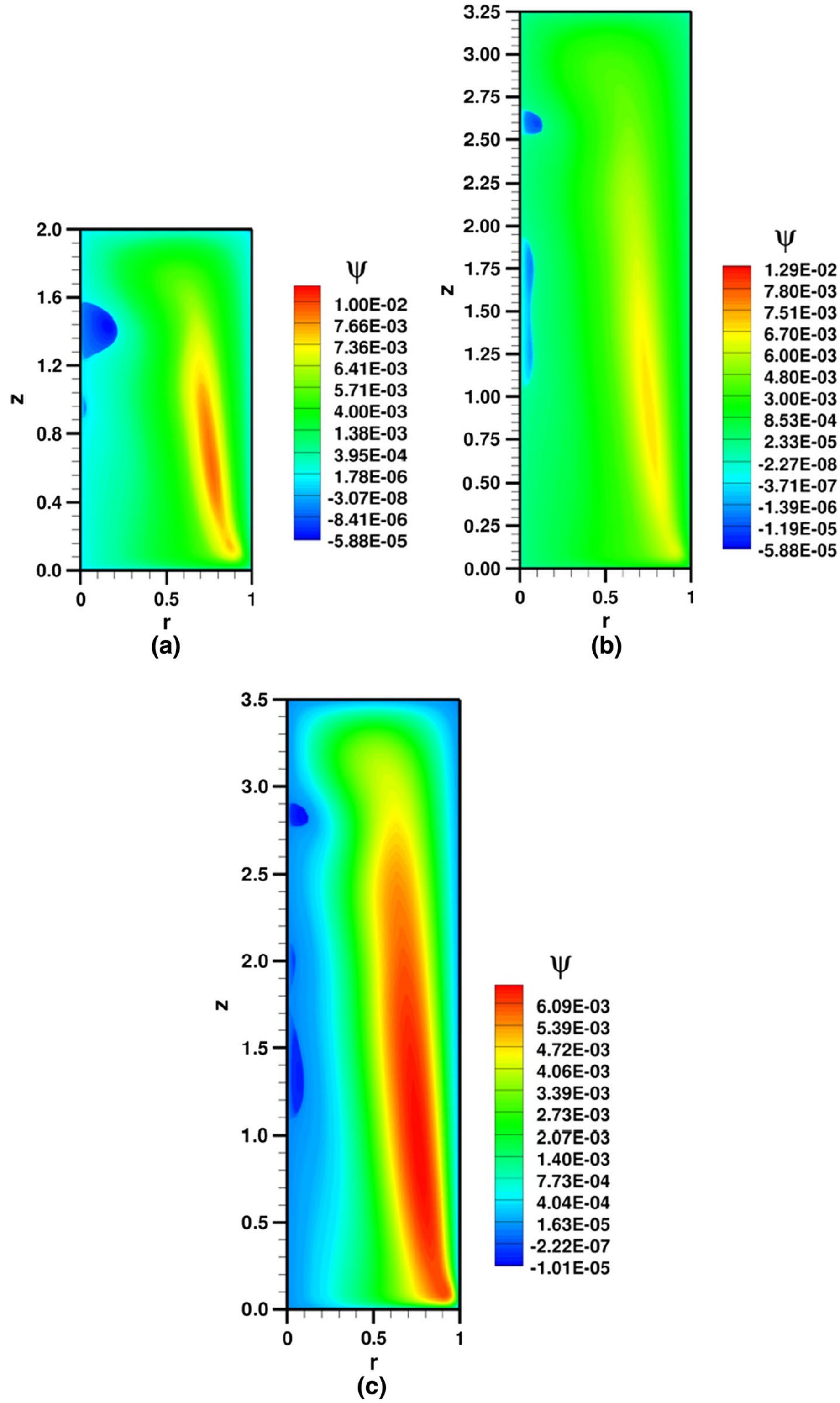

different Reynolds numbers (Re = 2000, 990 and 2819) and aspect ratios ($A = 1.0$, 1.5 and 3.25). Figure 7 analyzes the changes in the meridional flow due to co-rotation of the end walls with the same angular velocity. As previously observed by Bhattacharyya and Pal [14], the flow fields are symmetric in the top and bottom halves of the meridional plane. Also, there is a recirculation zone close to the rotation axis. For Re = 2819 and $A = 3.25$, it can be noticed a sharp slope of this rotation zone toward the cavity side wall.

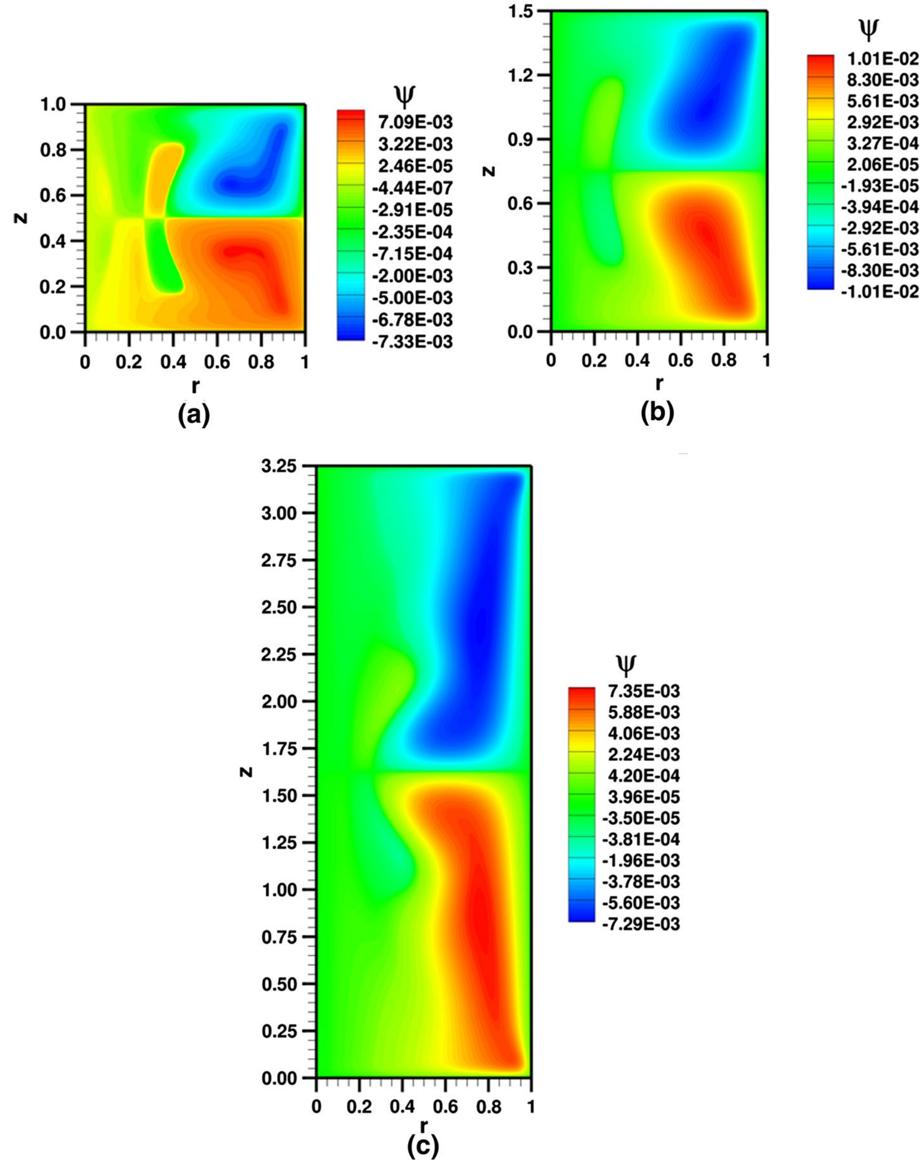

Fig. 7 Streamfunction patterns due to co-rotation ($s_u = s_b = 1$): **a** Re = 2000 and $A = 1.0$; **b** Re = 990 and $A = 1.5$; **c** Re = 2819 and $A = 3.25$

Figure 8 shows the flow characteristics, as obtained by the GITT approach, when upper and lower end walls rotate with opposite angular velocities of equal magnitude. Once again, it can be observed two symmetric regions about the mid plane (at $z = 1/2$) of counter rotating fluid, as previously indicated by Bhattacharyya and Pal [14]. Moreover, no breakdown bubble is observed for the counter rotating end walls case. It can be seen that for higher Reynolds number the streamline contours exhibit a more marked waviness. This flow pattern is characterized by the detachment of the separation vortex bubbles of the cylinder axes and the formation of two vortex rings. These separation zones appear when the streamfunction is null, developing a shear layer along the middle plane.

5 Conclusions

The laminar rotating end-driven flow in a closed cylindrical cavity has been investigated by the Generalized Integral Transform Technique (GITT). The subroutine BVPFD from the IMSL Library [51], which solves parametrized ordinary differential equations with boundary conditions at two points, was utilized for the numerical part of the hybrid approach, and the calculated results were compared with both numerical and experimental data available in the literature, with excellent overall agreement. The convergence analysis on the streamfunction, axial, radial and tangential velocity components demonstrates the excellent convergence rates, with fairly low required truncation orders in the eigenfunction expansions (i.e., N = NF = NV ≤ 90). The overall agreement of the GITT solution with the experimental

Fig. 8 Streamfunction patterns due to counter-rotation ($s_u = 1$ and $s_b = -1$): **a** Re = 2000 and $A = 1.0$; **b** Re = 990 and $A = 1.5$; **c** Re = 2819 and $A = 3.25$

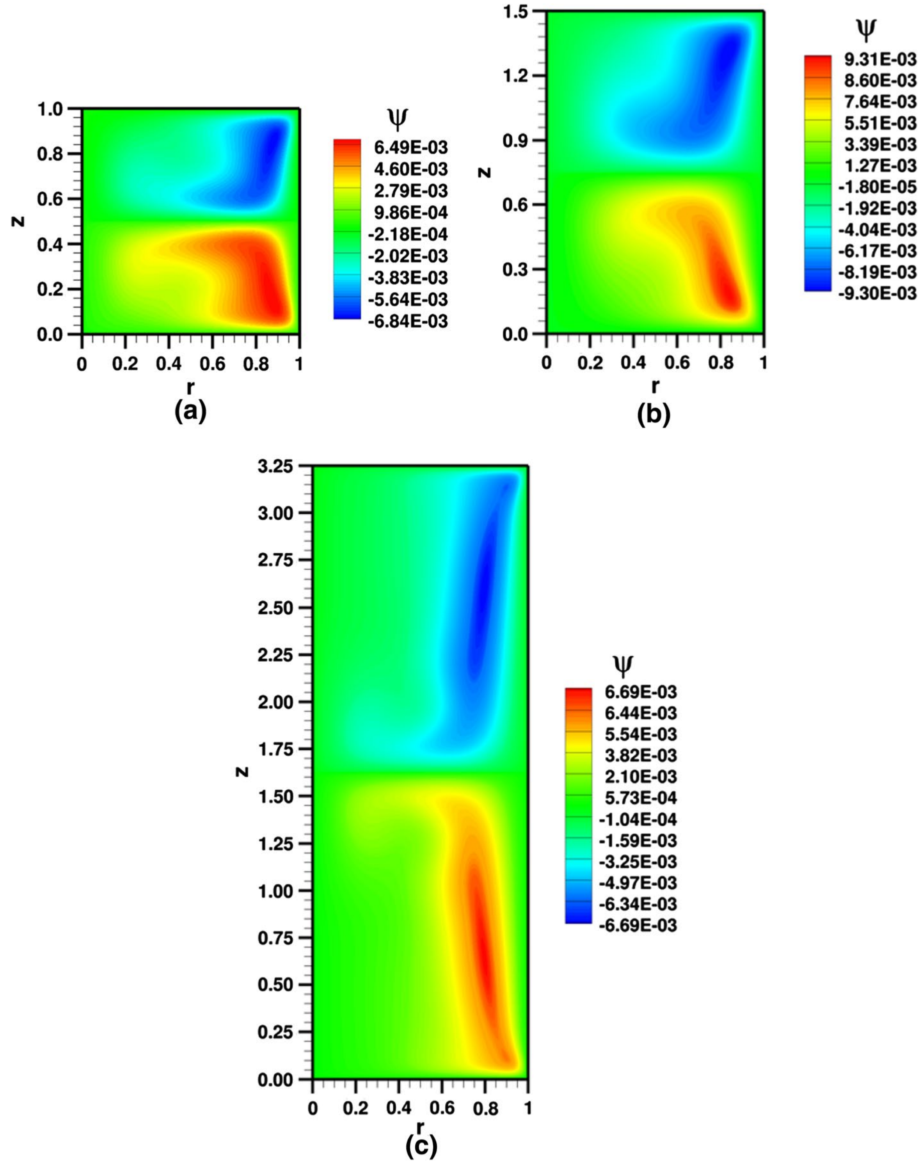

results [15] for the maximum velocity component is also illustrated. Moreover, the physical behavior of the computed axial and radial velocity components, and consequently the streamfunction, was consistent with the flow visualizations in terms of the position and size of breakdown bubbles, as from the work of Escudier [4]. Results presented for co- and counter-rotation of the end walls for different Reynolds numbers and aspect ratios show that the flow pattern is characterized by the formation of two symmetric regions about the mid plane of the rotating fluid and are in accordance with the results in the literature [14].

Acknowledgements The authors acknowledge the financial support by CAPES/PROCAD, CNPq and FAPERJ, all of them research sponsoring agencies in Brazil.

References

1. Leibovich S (1978) The structure of vortex breakdown. Ann Rev Fluid Mech 10:221–246
2. Pao HP (1970) A numerical computation of a confined rotating flow. J Appl Mech 37:480–487
3. Pao HP (1972) Numerical solution of the Navier-Stokes equations for flows in the disk-cylinder system. Phys Fluids 15:4–11
4. Escudier MP (1984) Observations of the flow produced in a cylindrical container by a rotating endwall. Exp Fluids 2:189–196
5. Hall MG (1972) Vortex breakdown. Annu Rev Fluid Mech 4:195–218
6. Escudier MP (1988) Vortex breakdown: observations and explanations. Prog Aerosp Sci 25:189–229
7. Delery JM (1994) Aspects of vortex breakdown. Prog Aerosp Sci 30:1–59
8. Lucca-Negro O, O'Doherty T (2001) Vortex breakdown: a review. Prog Energy Combust Sci 27:431–481

9. Lopez JM (1990) Axisymmetric vortex breakdown part 1: confined swirling flow. J Fluid Mech 221:533–552
10. Spohn A, Mory M, Hopfinger EJ (1993) Observations of vortex breakdown in an open cylindrical container with a rotating bottom. Exp Fluids 14:70–77
11. Valentine DT, Jahnke CC (1994) Flows induced in a cylinder with both end walls rotating. Phys Fluids 6:2702–2710
12. Gelfgat AY, Bar-Yoseph PZ, Solan A (1996) Steady states and oscillatory instability of swirling flow in a cylinder with rotating top and bottom. Phys Fluids 8:2614–2625
13. Jankhe CC, Valentine DT (1998) Recirculation zones in a cylindrical container. J Fluids Eng 120:680–684
14. Bhattacharyya S, Pal A (1999) On the flow between two rotating disks enclosed by a cylinder. Acta Mech 135:27–40
15. Fujimura K, Yoshizawa H, Iwatsu R, Koyama HS, Hyun JM (2001) Velocity measurements of vortex breakdown in an enclosed cylinder. J Fluids Eng 123:604–611
16. Bhaumik SK, Lakshmisha KN (2007) Lattice Boltzmann simulation of lid-driven swirling flow in confined cylindrical cavity. Comput Fluids 36:1163–1173
17. Guo Z, Han H, Shi B, Zheng C (2009) Theory of the Lattice Boltzmann equation: Lattice Boltzmann model for axisymmetric flows. Phys Rev E 79:046708-2-046708–12
18. Zhang T, Shi B, Chai Z, Rong F (2012) Lattice BGK model for incompressible axisymmetric flows. Commun Comput Phys 11:1569–1590
19. Gelfgat AY (2015) Primary oscillatory instability in a rotating disk-cylinder system with aspect (height/radius) ratio varying from 0.1 to 1. Fluid Dyn Res 47:035502-1-035502–14
20. Dash SC, Singh N (2018) Stability boundaries for vortex breakdowns and boundaries between oscillatory and steady swirling flow in a cylindrical annulus with a top rotating lid. J Brazil Soc Mech Sci Eng 40:336
21. Xiao M, Dou HS, Wu C, Zhu Z, Zhao X, Chen S, Chen H, Wei Y (2018) Analysis of vortex breakdown in an enclosed cylinder based on the energy gradient theory. Eur J Mech B Fluids 71:66–76
22. Erkinjon Son MM (2020) Numerical calculation of an air centrifugal separator based on the SARC turbulence model. J Appl Comput Mech 6(SI):1133–1140
23. Cotta RM (1990) Hybrid numerical-analytical approach to nonlinear diffusion problems. Numer Heat Transf Part B Fundam 17:217–226
24. Serfaty R, Cotta RM (1992) Integral transform solutions of diffusion problems with nonlinear equation coefficients. Int Commun Heat Mass Transf 17(6):851–864
25. Serfaty R, Cotta RM (1992) Hybrid analysis of transient nonlinear convection-diffusion problems. Int J Numer Methods Heat Fluid Flow 2:55–62
26. Cotta RM (1993) Integral transforms in computational heat and fluid flow. CRC Press, Boca Raton
27. Cotta RM (1994) Benchmark results in computational heat and fluid flow: the integral transform method. Int J Heat Mass Transf 37:381–394
28. Cotta RM, Mikhailov MD (2006) Hybrid methods and symbolic computations. In: Minkowycz WJ, Sparrow EM, Murthy JY (eds) Handbook of numerical heat transfer, 2nd edn. John Wiley, New York, pp 493–522
29. Cotta RM, Knupp DC, Lisboa KM, Naveira-Cotta CP, Quaresma JNN, Zotin JLZ, Miyagawa HK (2020) Integral transform benchmarks of diffusion, convection-diffusion, and conjugated problems in complex domains. In: Runchal AK (ed) 50 Years of CFD in engineering sciences: a commemorative volume in memory of D. Brian Spalding. Springer, Berlin, pp 719–750
30. Perez-Guerrero JS, Cotta RM (1992) Integral transform solution for the lid-driven cavity flow problem in streamfunction-only formulation. Int J Numer Methods Fluids 15:399–409
31. Perez-Guerrero JS, Cotta RM (1995) Integral transform solution of developing laminar duct flow in Navier-Stokes formulation. Int J Numer Methods Fluids 20:1203–1213
32. Perez-Guerrero JS, Cotta RM (1996) Benchmark integral transform results for flow over a backward-facing step. Comput Fluids 25:527–540
33. Lima JA, Perez-Guerrero JS, Cotta RM (1997) Hybrid solution of the averaged Navier-Stokes equations for turbulent flow. Comput Mech 19:297–307
34. Quaresma JNN, Cotta RM (1997) Integral transform method for the Navier-Stokes equations in steady three-dimensional flow. In: Proceedings of the 10th ISTP—International symposium on transport phenomena, vol 1. Kyoto, Japan, pp 281–287
35. Pereira LM, Perez-Guerrero JS, Cotta RM (1998) Integral transformation of the Navier-Stokes equations in cylindrical geometry. Comput Mech 21:60–70
36. Pereira LM, Cotta RM, Perez-Guerrero JS (2000) Analysis of laminar forced convection in annular ducts using integral transforms. Hybrid Methods Eng 2:221–232
37. Pereira LM, Perez-Guerrero JS, Brazão N, Cotta RM (2002) Compressible flow and heat transfer in ultracentrifuges: hybrid analysis via integral transforms. Int J Heat Mass Transf 45:99–112
38. Leal MA, Perez-Guerrero JS, Cotta RM (1999) Natural convection inside two-dimensional cavities: the integral transform method. Int J Numer Methods Biomed Eng 15:113–125
39. Leal MA, Machado HA, Cotta RM (2000) Integral transform solutions of transient natural convection in enclosures with variable fluid properties. Int J Heat Mass Transf 43:3977–3990
40. Perez-Guerrero JS, Quaresma JNN, Cotta RM (2000) Simulation of laminar flow inside ducts of irregular geometry using integral transforms. Comput Mech 25:413–420
41. Ramos R, Perez-Guerrero JS, Cotta RM (2001) Stratified flow over a backward facing step: hybrid solution by integral transforms. Int J Numer Methods Fluids 35:173–197
42. Lima GGC, Santos CAC, Haag A, Cotta RM (2007) Integral transform solution of internal flow problems based on Navier-Stokes equations and primitive variables formulation. Int J Numer Methods Eng 69:544–561
43. Silva CAM, Macêdo EN, Quaresma JNN, Pereira LM, Cotta RM (2010) Integral transform solution of the Navier-Stokes equations in full cylindrical regions with streamfunction formulation. Int J Numer Methods Biomed Eng 26:1417–1434
44. Matt CFT, Quaresma JNN, Cotta RM (2017) Analysis of magnetohydrodynamic natural convection in closed cavities through integral transforms. Int J Heat Mass Transf 113:502–513
45. Lisboa KM, Cotta RM (2018) Hybrid integral transforms for flow development in ducts partially filled with porous media. Proc R Soc A Math Phys Eng Sci 474:20170637-1-20170637–20
46. Lisboa KM, Su J, Cotta RM (2019) Vector eigenfunction expansion in the integral transform solution of transient natural convection. Int J Numer Methods Heat Fluid Flow 29:2684–2708
47. Cotta RM, Lisboa KM, Curi MF, Balabani S, Quaresma JNN, Perez-Guerrero JS, Macêdo EN, Amorim NS (2019) A review of hybrid integral transform solutions in fluid flow problems with heat or mass transfer and under Navier-Stokes equations formulation. Numer Heat Transf Part B Fundam 76:60–87
48. Miyagawa HK, Quaresma JNN, Lisboa KM, Cotta RM (2020) Integral transform analysis of convective heat transfer within wavy walls channels. Numer Heat Transf Part A Appl 77(5):460–481
49. Quaresma JNN, Cruz CCS, Cagney N, Cotta RM, Balabani S (2020) Effect of mixed convection on laminar vortex breakdown in a cylindrical enclosure with a rotating bottom plate. Int J Therm Sci 155:106399-1-106399–14

50. Pinheiro IF, Puccetti G, Morini GL, Sphaier LA (2021) Integral transform analysis of microchannel fluid flow: irregular geometry estimation using velocimetry data. Appl Math Model 90:943–954
51. IMSL® (2018) Fortran numerical library version 2018. Rogue Wave Software Incorporation, Boulder